Microsystem Technologies (2022) 28:1637–1651
https://doi.org/10.1007/s00542-022-05303-x

TECHNICAL PAPER

Shape optimization of piezoelectric energy harvesters based on isogeometric analysis and particle swarm optimization

Yajun Cao[1] · Huaiwei Huang[1]

Received: 29 July 2021 / Accepted: 17 April 2022 / Published online: 18 May 2022
© The Author(s), under exclusive licence to Springer-Verlag GmbH Germany, part of Springer Nature 2022

Abstract
Shape optimization of piezoelectric energy harvesters (PEH) is deemed to be one of the most effective methods to enhance energy efficiency. In this paper, we propose a novel shape optimization approach for PEH by combining isogeometric analysis (IGA) and particle swarm optimization (PSO). Based on the Kirchhoff–Love plate theory and Hamilton's principle, an IGA formula is modeled for a bimorph PEH. Meanwhile, two optimization models with maximum average open-circuit voltage as the objective function are established, and the difference between the two is whether frequency constraint is considered or not. Then, we set the coordinates of control points to be design variables and utilize PSO to solve optimization problems. The numerical examples are performed to verify the accuracy and convergence of the IGA model and systematically compare the computational efficiency between PSO and genetic algorithm (GA). Furthermore, the shape optimization is executed for three different structures, and the effect of thickness ratio and frequency constraint on the optimized shapes are further analyzed. The results show that maximum output power and power density of the optimized design respectively increase by 184.7 and 36.4%, compared with the initial design. More importantly, the presented method can realize the integrated analysis of modeling, simulation, and optimization for PEH.

1 Introduction

Shape optimization refers to optimizing the shape of the geometric structure to make it have more excellent mechanical properties. Traditional shape optimization usually bases on the finite element method to solve the structural response, and the nodes on the boundary are defined as design variables (Francavilla et al. 1975). However, due to irregular boundaries and geometric errors between the design model and the analysis model, such definition often leads to non-physical design. To improve the smoothness of the geometric boundary, the polynomial and spline functions were proposed to characterize the structure boundary (Bhavikatti and Ramakrishnan 1980). Among them, spline functions, such as B-splines and Non-uniform Rational B-splines (NURBS) basis functions, can eliminate the oscillation boundary and have a relatively higher local smoothness, which attract wide attention (Piegl and Tiller 1997).

To seamlessly integrate the geometric model and the analysis model, Hughes et al. (2005) introduced isogeometric analysis (IGA). The fundamental principle of IGA is that the NURBS basis functions used in the geometric model are employed as shape functions to approximate the unknown field. Because of its accurate description of the geometric model and high-order continuity, many works have been done to analyze piezoelectric structure. For example, Willberg and Gabbert (2012) first presented a three-dimensional electromechanical-coupled isogeometric element, and the functionality and the advantages of the isogeometric element were demonstrated by simulating piezoelectric sensor and actuator. Next, the static, free vibration, and dynamic control of piezoelectric composite plates based on shear deformation theory were studied (Phung-Van et al. 2015a). The similar work was also extended to carbon nanotube reinforced composite nanoplates (Thanh et al. 2018; Nguyen-Quang et al. 2018), functionally graded plates (Liu et al. 2020), and laminated composite shells (Nikoei and Hassani 2019, 2020). Inspired by the above works, Van et al. (2015b) considered using GA to optimize the input voltage for active control.

✉ Huaiwei Huang
cthwhuang@scut.edu.cn

[1] School of Civil Engineering and Transportation, South China University of Technology, Guangzhou, Guangdong 510640, People's Republic of China

Considering that piezoelectric structure has broad application prospect in the field of health monitor, researchers also focus on its wave characteristic (Li et al. 2020; Li and Han 2020; Liu et al. 2019) and crack evolution (Benson et al. 2010; Bui 2015; Bui et al. 2016; Singh and Singh 2020). Moreover, Akbar and Curiel-Sosa (2018) implemented a hybrid mathematical/IGA scheme to evaluate PEH. However, the output voltage cannot be computed directly, because the model did not use of a fully coupled electromechanical element.

According to the literature survey, some researchers have studied topology optimization (Kumar and Parthasarathy 2011) and shape optimization (Wall et al. 2008) by using IGA. The core idea of isogeometric shape optimization is to define the control points as design variables, and the key of solving the problem lie in the sensitivity formula. Cho and Ha (2009) derived an enhanced shape sensitivity and proved that the continuity of the normal vector and curvature was important over the whole design domain. Later on, this method was utilized in the shape optimization of built-up structures, and the effect of exact curvature on the design sensitivity was further demonstrated (Lee and Cho 2015). To reduce the complexity of the sensitivity formula for the shell components, Kiendl et al. (2014) presented sensitivity weighting and semi-analytical sensitivity. Ha et al. (2015) proposed a generalized sensitivity formula described in a curvilinear coordinated system, which overcame the boundary resultants accompanying severe curvature changes. Furthermore, there are currently two methods to improve the shape flexibility of the geometric model. The first method is to define both the positions and weights of the NURBS control points as design variables (Qian 2010). The other is the trimming technique (Seo et al. 2010), which can complete shape and topology optimization for shell structure simultaneously. With the continuous development of the method, isogeometric shape optimization has been used for minimum complementary strain energy (Nagy et al. 2010a), stress constraint problem (Nagy et al. 2010b), maximum buckling load factor (Nagy et al. 2013), and heat conduction problem (Yoon et al. 2015). In this paper, the research progress of isogeometric topology optimization is not reviewed, and interested readers can refer to the review articles (Wang et al. 2018; Gao et al. 2020).

Above-mentioned isogeometric shape optimization usually utilizes gradient-based methods to solve optimization problems. However, gradient-based methods require sensitivity data, which are difficult to derive and implement for some special problems. Therefore, the gradient-free methods have also aroused researchers' interest, especially the rapid development of artificial intelligence algorithms in recent years. For instance, Sun et al. (2018) developed a shape optimization approach based on the isogeometric boundary element method and particle swarm optimization (PSO). Subsequently, this approach was expanded to the shape optimization of the two-dimensional Helmholtz acoustic problems (Mostafa Shaaban et al. 2020). Truong et al. (2021) realized the material distribution optimization of two-dimensional functionally graded beams by using the deep feedforward neural network and PSO. The obtained results show its accuracy and effectiveness. In summary, the use of PSO for isogeometric shape optimization not only provides an attractive gradient-free option, but also has the characteristics of high accuracy and effectiveness.

To the best of our knowledge, a few works consider the shape optimization of piezoelectric energy harvester (PEH) to enhance energy efficiency. On the one hand, the parameter analysis was implemented based on the theoretical model and simulation study, where the effect of geometric parameters such as proof mass shapes (Nisanth et al. 2021), structural dimensions (Ghoddus and Kordrostami 2018) and thickness profile (Kundu and Nemade 2021) on the performance of the traditional PEH were analyzed, and optimized values were obtained for higher output power. On the other hand, one utilized exponential function or polynomial function to describe the structure boundary, and applied heuristic algorithm (Dietl and Garcia 2010), artificial immune system (Tabatabaei et al. 2016) and ant colony system (Salmani et al. 2019) to obtain optimized shape parameters. However, the above works are based on theoretical analysis and simulation study, which is not conductive to the shape optimization of complex geometry.

Recently, IGA was utilized to evaluate the performance of PEH with arbitrarily complex structure, and the parametric analysis to investigate the effect of shape perturbations and tip mass on the fundamental frequency and voltage amplitude was conducted (Peralta et al. 2020). The authors extended the above works to variable thickness PEH and proposed a multi-objective Kriging metamodel to perform shape optimization (Calderon Hurtado et al. 2022). However, the input–output database with 30,000 support points was utilized to ensure the high accuracy of the metamodel. Therefore, to save computational cost and realize the integrated analysis of modeling, simulation and shape optimization of PEH, this paper proposes a shape optimization approach based on IGA and PSO.

The remainder of this paper is organized as follows. The isogeometric framework of the model is presented in Sect. 2. Section 3 proposes two different optimization models for PEH and briefly reviews PSO. In Sect. 4, numerical results are validated against the data from the literature, and the convergence analysis is displayed. Eventually, some numerical examples about the shape optimization of PEH are employed to show the

effectiveness of the presented method. Conclusions are described in Sect. 5.

2 Isogeometric formulation for PEH

In this paper, a bimorph PEH with width b and length L is considered, as shown in Fig. 1. The upper and lower layers are piezoelectric material with thickness h_p. The middle layer is metal material with thickness h_s. $x-y$ plane is defined in the neutral plane of the plate. It is assumed that the polarization directions of the piezoelectric layers are opposite, and a series connection can be utilized to harvest energy. The Kirchhoff–Love plate theory and IGA are integrated to develop a numerical approach for PEH, and the related equations of PEH subjected to harmonic excitation are represented in this section.

2.1 The B-splines and NURBS basis functions

For the completeness of the paper, we briefly review the concept of the NURBS basis functions, and the work (Hughes et al. 2005) can be referred to attain more detailed introduction. In brief, a non-decreasing knot vector $\Xi = \{\xi_1, \xi_2, ..., \xi_i, ..., \xi_{n+p+1}\}$ is utilized to construct the B-splines basis functions in the parameter space with $0 \le \xi \le 1$, where ξ_i is the ith knot; i is the knot index; n is the number of basis functions, and p is the polynomial order. Giving a knot vector, the B-splines basis functions are expressed by the Cox-De Boor recursive formula

$$\begin{aligned} N_{i,0}(\xi) &= \begin{cases} 1, \ if \ \xi_i \le \xi < \xi_{i+1} \\ 0, \ else \end{cases} \\ N_{i,p}(\xi) &= \frac{\xi - \xi_i}{\xi_{i+p} - \xi_i} N_{i,p-1}(\xi) \\ &+ \frac{\xi_{i+p+1} - \xi}{\xi_{i+p+1} - \xi_{i+1}} N_{i+1,p-1}(\xi) \, for \, p \ge 1 \end{aligned} \tag{1}$$

According to the tensor product, two-dimensional NURBS basis functions are obtained as follows

$$R_{i,j}^{p,q}(\xi,\eta) = \frac{w_{i,j} N_{i,p}(\xi) M_{j,q}(\eta)}{\sum_{\hat{i}=1}^{n} \sum_{\hat{j}=1}^{m} N_{\hat{i},p}(\xi) M_{\hat{j},q}(\eta) w_{\hat{i},\hat{j}}} \tag{2}$$

where $w_{i,j}$ is the weight, $N_{i,p}(\xi)$ and $M_{j,q}(\eta)$ represent the B-splines basis functions defined in the ξ and η directions with knot vectors $\Xi_\xi = \{\xi_1, \xi_2, \ldots, \xi_i, \ldots \xi_{n+p+1}\}$ and $\Xi_\eta = \{\eta_1, \eta_2, \ldots, \eta_j, \ldots \eta_{m+q+1}\}$, respectively.

2.2 Kirchhoff–Love plate theory

Considering the Kirchhoff–Love plate theory, the displacement equations along three directions are written as

$$\begin{aligned} u_1(x,y,t) &= u(x,y,t) - z\frac{\partial w(x,y,t)}{\partial x} \\ u_2(x,y,t) &= v(x,y,t) - z\frac{\partial w(x,y,t)}{\partial y} \\ u_3(x,y,t) &= w(x,y,t) \end{aligned} \tag{3}$$

where $u(x,y,t), v(x,y,t)$ and $w(x,y,t)$ are the displacements of the neutral plane in x, y and z direction. The mechanical strain fields are obtained

$$S_{ij} = \frac{1}{2}\left(u_{i,j} + u_{j,i}\right) \tag{4}$$

According the Kirchhoff hypothesis, the corresponding in-plane strain components can be written as

$$S_1 = \frac{\partial u_1}{\partial x}, S_2 = \frac{\partial u_2}{\partial y}, S_{12} = \frac{\partial u_1}{\partial y} + \frac{\partial u_2}{\partial x} \tag{5}$$

where S_1 and S_2 are axial strain along x and y directions, and S_{12} is shear strain. Substituting Eq. (3) into Eq. (5), and the strain components can be expressed in a compact notation

$$S = S_m + zS_b \tag{6}$$

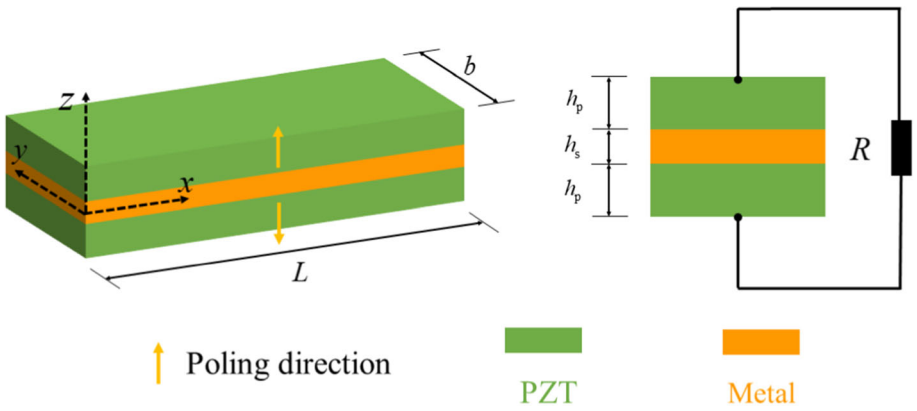

Fig. 1 Schematic diagram of a bimorph PEH

where $S_m = \left[\frac{\partial u}{\partial x} \quad \frac{\partial v}{\partial y} \quad \frac{\partial u}{\partial y}+\frac{\partial v}{\partial x}\right]^T$, $S_b = \left[-\frac{\partial^2 w}{\partial x^2} \quad -\frac{\partial^2 w}{\partial y^2} \quad -2\frac{\partial^2 w}{\partial x \partial y}\right]^T$.

In general, piezoelectric materials are usually transversely isotropic materials, such as PZT-5H and PZT-5A. According to IEEE Standard on piezoelectricity (American and Standard 1984), $x-y$ plane is isotropic, and the polarization direction of the piezoelectric material is along z direction. Therefore, the constitutive equation describing the piezoelectric effect can be written as

$$\begin{aligned} T_{ij} &= C_{ijkl}S_{kl} - e_{kij}E_k \\ D_i &= e_{ikl}S_{kl} + \varepsilon_{ik}^S E_k \end{aligned} \tag{7}$$

herein, T represents the stress tensor, and E, D respectively denote the electric filed and the electric displacement. The elastic tensor C in matrix form is formulated as

$$C = \begin{bmatrix} c_{11} & c_{12} & c_{13} & 0 & 0 & 0 \\ c_{21} & c_{22} & c_{23} & 0 & 0 & 0 \\ c_{31} & c_{32} & c_{33} & 0 & 0 & 0 \\ 0 & 0 & 0 & c_{44} & 0 & 0 \\ 0 & 0 & 0 & 0 & c_{55} & 0 \\ 0 & 0 & 0 & 0 & 0 & c_{66} \end{bmatrix} \tag{8}$$

The third-order piezoelectric tensor e representing the mechanical-electric coupling effect and the second-order electric permittivity tensor ε^S in matrix form are expressed as

$$\begin{aligned} e &= \begin{bmatrix} 0 & 0 & 0 & 0 & e_{15} & 0 \\ 0 & 0 & 0 & e_{24} & 0 & 0 \\ e_{31} & e_{32} & e_{33} & 0 & 0 & 0 \end{bmatrix}, \\ \varepsilon^S &= \begin{bmatrix} \varepsilon_{11}^S & 0 & 0 \\ 0 & \varepsilon_{22}^S & 0 \\ 0 & 0 & \varepsilon_{33}^S \end{bmatrix} \end{aligned} \tag{9}$$

in which $e_{31} = e_{32}, e_{24} = e_{15}, \varepsilon_{11}^S = \varepsilon_{22}^S$, and the contracted notation is used (i.e., Voigt's notation: $11 \to 1, 22 \to 2, 33 \to 3, 23 \to 4, 13 \to 5, 12 \to 6$). The middle layer is considered as an isotropic material, and the corresponding constitutive relation holds $T = C_s S$.

2.3 The isogeometric discretization and govering equations

According to isogeometric discretization, the displacement fields u, v, w are approximated by the NURBS basis function

$$\mathbf{u}_0 = \sum_{i=1}^{n\times m} R_i \mathbf{u}_i \tag{10}$$

where $\mathbf{u}_i = [u_i \quad v_i \quad w_i]^T$. We substitute Eq. (10) into the Eq. (6) and obtain

$$S_m = B_m \mathbf{u}, S_b = B_b \mathbf{u} \tag{11}$$

here $\mathbf{u}$ represents the displacements of all control points,

$$B_m = \begin{bmatrix} R_{i,x} & 0 & 0 \\ 0 & R_{i,y} & 0 \\ R_{i,y} & R_{i,x} & 0 \end{bmatrix}, B_b = \begin{bmatrix} 0 & 0 & -R_{i,xx} \\ 0 & 0 & -R_{i,yy} \\ 0 & 0 & -2R_{i,xy} \end{bmatrix}.$$

It is assumed that each element in the piezoelectric domain defines a degree of freedom of electric potential. The electric field can be expressed as $E = -B_\phi \phi_e$, where $B_\phi = 1/(2h_p)$, and ϕ_e represents the electric potential of eth element. According to Hamilton's principle, the weak form of the problem is given by (Peralta et al. 2020)

$$\begin{aligned} \int_{t_1}^{t_2} \Bigg\{ \int_{-h/2}^{h/2} \Bigg[\int_\Omega \rho \delta \dot{\boldsymbol{u}}^T \dot{\boldsymbol{u}} \mathrm{d}\Omega - \int_\Omega \delta S^T T \mathrm{d}\Omega \\ + \int_\Omega \delta E^T D \mathrm{d}\Omega + \int_\Omega \delta \boldsymbol{u}^T f_b \mathrm{d}\Omega \Bigg] \mathrm{d}z + \int_\Omega \delta \phi_e^T \overline{q} \mathrm{d}\Omega \Bigg\} \mathrm{d}t = 0 \end{aligned} \tag{12}$$

substituting constitutive relation, Eq. (12) is rewritten as

$$\begin{aligned} \int_{t_1}^{t_2} \Bigg\{ \int_{-h/2}^{h/2} \Bigg[\int_\Omega \rho \delta \dot{\boldsymbol{u}}^T \dot{\boldsymbol{u}} \mathrm{d}\Omega - \int_\Omega \delta S^T T \mathrm{d}\Omega + \int_\Omega \delta S^T e^T E \mathrm{d}\Omega \\ + \int_\Omega \delta E^T e S \mathrm{d}\Omega. + \int_\Omega \delta E^T \varepsilon^S E \mathrm{d}\Omega + \int_\Omega \delta \boldsymbol{u}^T f_b \mathrm{d}\Omega \Bigg] \mathrm{d}z + \int_\Omega \delta \phi_e^T \overline{q} \mathrm{d}\Omega \Bigg\} \mathrm{d}t = 0 \end{aligned} \tag{13}$$

where ρ is material density; f_b is the body load; $\overline{q}$ represents the surface electrical charge; δ denotes the variation operator, and the notion $\dot{\Xi}$ means $\partial \Xi / \partial t$. Substituting displacement, strain, and electric field equations into Eq. (13) and assembling the element matrix, the global governing formulations are subsequently written by

$$\begin{aligned} M_{uu}\ddot{\mathbf{u}} + C_{uu}\dot{\mathbf{u}} + K_{uu}\mathbf{u} + K_{u\phi}\phi &= f \\ K_{\phi u}\mathbf{u} - K_{\phi\phi}\phi &= Q \end{aligned} \tag{14}$$

where

$$M_{uu}=\int_{\Omega}\left(\mathrm{N}_1^T m_0 \mathrm{N}_1+\mathrm{N}_2^T m_1 \mathrm{N}_1+\mathrm{N}_1^T m_1 \mathrm{N}_2+\mathrm{N}_2^T m_2 \mathrm{N}_2\right)\mathrm{d}\Omega, K_{uu}=\int_{\Omega}\left(B_m^T A B_m+B_b^T B B_m+B_m^T B B_b+B_b^T D B_b\right)\mathrm{d}\Omega$$

$$K_{u\phi}=\Theta\int_{\Omega_\mathrm{p}}\left(B_b^T e^T B_\phi\right)\mathrm{d}\Omega_\mathrm{p}, K_{\phi\phi}=2h_\mathrm{p}\int_{\Omega_\mathrm{p}}\left(B_\phi^T \varepsilon^S B_\phi\right)\mathrm{d}\Omega_\mathrm{p}, f=\int_{\Omega}\left(\mathrm{N}_1^T \Gamma^T f_b\right)\mathrm{d}\Omega, C_{uu}=\alpha M_{uu}+\beta K_{uu}, Q=\int_{\Omega}\overline{q}\mathrm{d}\Omega$$

$$\Gamma=diag(h,h,h),\{\,m_0\quad m_1\quad m_2\,\}=\sum_{nl=1}^{3}(\rho)_{nl}\left\{\,(z_{nl}-z_{nl-1})\quad\left(z_{nl}^2-z_{nl-1}^2\right)/2\quad\left(z_{nl}^3-z_{nl-1}^3\right)/3\,\right\}$$

$$\Theta=\left(2h_s h_\mathrm{p}+h_\mathrm{p}^2\right),\{\,A\quad B\quad D\,\}=\sum_{nl=1}^{3}(C)_{nl}\left\{\,(z_{nl}-z_{nl-1})\quad\left(z_{nl}^2-z_{nl-1}^2\right)/2\quad\left(z_{nl}^3-z_{nl-1}^3\right)/3\,\right\}$$

$$\mathrm{N}_1=\begin{bmatrix}R_i & 0 & 0\\ 0 & R_i & 0\\ 0 & 0 & R_i\end{bmatrix},\mathrm{N}_2=\begin{bmatrix}0 & 0 & -R_{i,x}\\ 0 & 0 & -R_{i,y}\\ 0 & 0 & 0\end{bmatrix}$$

It is noted that α and β are Rayleigh damping factors that can be confirmed as follows (Erturk and Inman 2011)

$$\alpha=\frac{2\omega_1\omega_2(\omega_1\xi_2-\omega_2\xi_1)}{\omega_1^2-\omega_2^2},\beta=\frac{2(\omega_1\xi_1-\omega_2\xi_2)}{\omega_1^2-\omega_2^2} \tag{15}$$

in which ω_1,ω_2 are the first two natural frequency, and ξ_1,ξ_2 are corresponding damping ratio.

In the energy harvesting problem, in addition to displacement boundary conditions, electrical boundary condition need to be considered. Assuming that the electrodes are perfectly connected, the equipotential boundary condition $\phi=B\boldsymbol{\phi}$ can be applied, in which $\boldsymbol{\phi}$ is voltage; B is a unit vector with dimension $N_{\mathrm{all}}\times 1$ (Igura et al. 1995), and N_{all} is the total number of elements. Therefore, Eq. (14) is rewritten as

$$\begin{aligned}M_{uu}\ddot{\mathbf{u}}+C_{uu}\dot{\mathbf{u}}+K_{uu}\mathbf{u}+\overline{K}_{u\phi}\boldsymbol{\phi}&=f\\ \overline{K}_{\phi u}\mathbf{u}-\overline{K}_{\phi\phi}\boldsymbol{\phi}&=\overline{Q}\end{aligned} \tag{16}$$

where $\overline{K}_{u\phi}=K_{u\phi}B,\overline{K}_{\phi\phi}=B^T K_{\phi\phi}B,\overline{Q}=B^T Q$. If the based displacement w_b in the transversal direction is a harmonic form, the distributed force f will represent inertial effect due to the transverse acceleration, that is $f=-M_{uu}\ddot{w}_b$. It is assumed that the transversal acceleration is $\ddot{w}_b=W_b e^{\mathrm{i}\omega t}(\mathrm{i}=\sqrt{-1})$, and the unknown displacement and the output voltage are $\mathbf{u}=Ue^{\mathrm{i}\omega t},\boldsymbol{\phi}=\Phi e^{\mathrm{i}\omega t}$, where ω denotes harmonic excitation frequency. By differentiating the second formula of the Eq. (16) with respect to time, the governing equations for harmonic vibration are formulated as

$$\begin{aligned}-\omega^2 M_{uu}U+\mathrm{i}\omega C_{uu}U+K_{uu}U+\overline{K}_{u\phi}\Phi&=W_b r\\ \mathrm{i}\omega\overline{K}_{\phi u}U-\mathrm{i}\omega\overline{K}_{\phi\phi}\Phi&=\Phi/R\end{aligned} \tag{17}$$

where $r=-M_{uu}[\,1\quad\ldots\quad 1\,]^T$. The frequency response function of the output voltage subjected to unit excitation amplitude is derived by solving the Eq. (17)

$$\frac{\Phi}{W_b}=\mathrm{i}\omega\left(\mathrm{i}\omega\overline{K}_{\phi\phi}+1/R\right)^{-1}\overline{K}_{\phi u}\left[\left(-\omega^2 M_{uu}+\mathrm{i}\omega C_{uu}+K_{uu}\right)+\mathrm{i}\omega\left(\mathrm{i}\omega\overline{K}_{\phi\phi}+1/R\right)^{-1}\overline{K}_{u\phi}\overline{K}_{\phi u}\right]^{-1}r \tag{18}$$

Note that the above process can be extended to higher-order shear deformation theory model. Since this paper only considers the thin plate, the corresponding elastic properties can be written as

$$\begin{aligned}C_\mathrm{s}&=\frac{E_\mathrm{s}}{1-\nu_\mathrm{s}^2}\begin{bmatrix}1 & \nu_\mathrm{s} & 0\\ \nu_\mathrm{s} & 1 & 0\\ 0 & 0 & (1-\nu_\mathrm{s})/2\end{bmatrix},C_\mathrm{p}\\ &=\begin{bmatrix}\overline{c}_{11} & \overline{c}_{12} & 0\\ \overline{c}_{12} & \overline{c}_{22} & 0\\ 0 & 0 & \overline{c}_{66}\end{bmatrix}\end{aligned} \tag{19}$$

For piezoelectric material, mechanical-electric coupling matrix is $e=[\,\overline{e}_{31}\quad\overline{e}_{32}\quad 0\,]$, and the dielectric constant only consider $\overline{\varepsilon}_{33}^S$, where

$$\begin{aligned}&\overline{c}_{11}=c_{11}-\frac{(c_{13})^2}{c_{33}},\overline{c}_{12}=c_{12}-\frac{c_{13}c_{23}}{c_{33}},\\ &\overline{c}_{22}=c_{22}-\frac{(c_{23})^2}{c_{33}},\overline{c}_{66}=c_{66}\\ &\overline{e}_{31}=e_{31}-\frac{c_{13}e_{33}}{c_{33}},\overline{e}_{32}=e_{32}-\frac{c_{23}e_{33}}{c_{33}},\overline{\varepsilon}_{33}^S=\varepsilon_{33}^S+\frac{(e_{33})^2}{c_{33}}\end{aligned} \tag{20}$$

3 Optimization problem

3.1 Optimization model

In order to improve the energy efficiency of a given structure, one can define maximum average open-circuit voltage within the measured frequency range as the objective function (Townsend et al. 2019), and the corresponding mathematical model is written as

$$\begin{aligned} &\min\ c_1 = \frac{1}{120\pi}\int_{\omega_{oc}-60\pi}^{\omega_{oc}+60\pi} \Phi_{oc}(\omega)\mathrm{d}\omega \\ &\text{s.t.} -\omega^2 M_{uu}U + i\omega C_{uu}U + K_{uu}U + \overline{K}_{u\phi}\Phi = W_b r \\ &i\omega\overline{K}_{\phi u}U - i\omega\overline{K}_{\phi\phi}\Phi = \Phi/R \end{aligned} \tag{21}$$

where $\Phi_{oc}(\omega)$ denotes the open-circuit voltage, and ω_{oc} is open-circuit resonant frequency (Bourisli and Al-Ajmi 2010).

Previous studies show that traditional PEH only have high energy efficiency near the resonant frequency (Erturk and Inman 2009). However, there are different vibration frequencies in the real environment. To ensure that PEH has a high energy efficiency at a specified frequency, we introduce frequency constraint into the optimization model. Then the penalty function method is used to convert the problem into an unconstrained problem (Sun et al. 2018), and the optimization formula is specifically expressed as

$$\begin{aligned} &\min\ c_2 = \frac{1}{120\pi}\int_{\omega_{oc}-60\pi}^{\omega_{oc}+60\pi} \Phi_{oc}(\omega)\mathrm{d}\omega + \lambda\left(\left|\omega_{oc}-\omega_{obj}\right| - \delta\right) \\ &\text{s.t.} -\omega^2 M_{uu}U + \mathrm{i}\omega C_{uu}U + K_{uu}U + \overline{K}_{u\phi}\Phi = W_b r \\ &\mathrm{i}\omega\overline{K}_{\phi u}U - \mathrm{i}\omega\overline{K}_{\phi\phi}\Phi = \Phi/R \end{aligned} \tag{22}$$

where ω_{obj} and δ respectively represent the objective frequency and frequency difference, and λ denotes the penalty factor. It is noted that the continuous integral is replaced by a discrete sum, in our case, there are 30 equally spaced frequency points in the range of $[(\omega_{oc}-60\pi),(\omega_{oc}+60\pi)]$(Townsend et al. 2019).

3.2 Particle swarm optimization

The PSO algorithm is proposed by Kennedy and Eberhart (1995), which is inspired by the simplified social behavior of birds. In PSO algorithm, the basic process consists of three steps, namely, generating particles' position and velocity, velocity update, and finally position update. Here, the initial swarm of N particles is defined, where particles' position represents a candidate solution, and velocity is the magnitude and direction of particles' motion. Later, the swarm is promoted to obtain optimized solution by updating the velocity and position with the influence of the personal best position pbest_i^k and the global best position gbest^k, where pbest_i^k and gbest^k stand for the optimized position of ith particle and the optimized position of the overall particles in the kth step, respectively. Finally, the optimized particle is obtained until the convergence condition is satisfied. The new velocity and position of each particle at kth iteration are given as

$$\begin{aligned} v_i^{k+1} &= \tilde{\omega}v_i^k + c_1\mathrm{rand}_1^k\left(\mathrm{pbest}_i^k - x_i^k\right) + c_2\mathrm{rand}_2^k\left(\mathrm{gbest}^k - x_i^k\right) \\ x_i^{k+1} &= x_i^k + v_i^{k+1} \end{aligned} \tag{23}$$

where k denotes the current iteration step; $\tilde{\omega}$ is the inertia weight; $v_i^k \in [-v_{\max}, v_{\max}]$, $v_{\max}$ is the maximum velocity of a particle; c_1 and c_2 are learning factors; rand_1^k and rand_2^k are random numbers between 0 and 1. It is worth noting that the $\tilde{\omega}$ decreases linearly during the optimization (Fourie and Groenwold 2002), that is $\tilde{\omega} = \tilde{\omega}_{\max} - (\tilde{\omega}_{\max} - \tilde{\omega}_{\min})k/T_{\max}$, where $T_{\max}$ is the maximum iteration step, and $\tilde{\omega}_{\min}, \tilde{\omega}_{\max}$ are the initial and final inertia weights. The optimization flow chart is shown in the Fig. 2.

4 Numerical analysis

In this section, the IGA model is verified by comparing with the results obtained from literature, and the convergence analysis is performed in terms of the relationship between the accuracy of the first natural frequency and the number of elements. The comparative analysis is made among PSO and GA to highlight PSO's convergence speed and computational efficiency. The shape optimization of three different structures is examined based on the optimization model defined in Sect. 3.1, and the effect of thickness ratio and frequency constraint on optimized designs is investigated systematically. Unless otherwise stated, the piezoelectric material is PZT-5H, and the matrix material is Brass. Table 1 shows the material properties.

4.1 Validation and convergence analysis

Referring to the experimental model (Erturk and Inman 2011), the geometric dimensions are set as $L = 24.53$ mm, $b = 6.4$ mm, $h_p = 0.265$ mm, $h_s = 0.14$ mm, and the damping ratio is $\xi_1 = 0.00874$. The resistance $R = 470\Omega$, and the amplitude of excitation acceleration is 1 m/s^2. The structure is discretized into 16×16 quadratic elements. Figure 3 shows the frequency response of the output voltage including the experimental values,

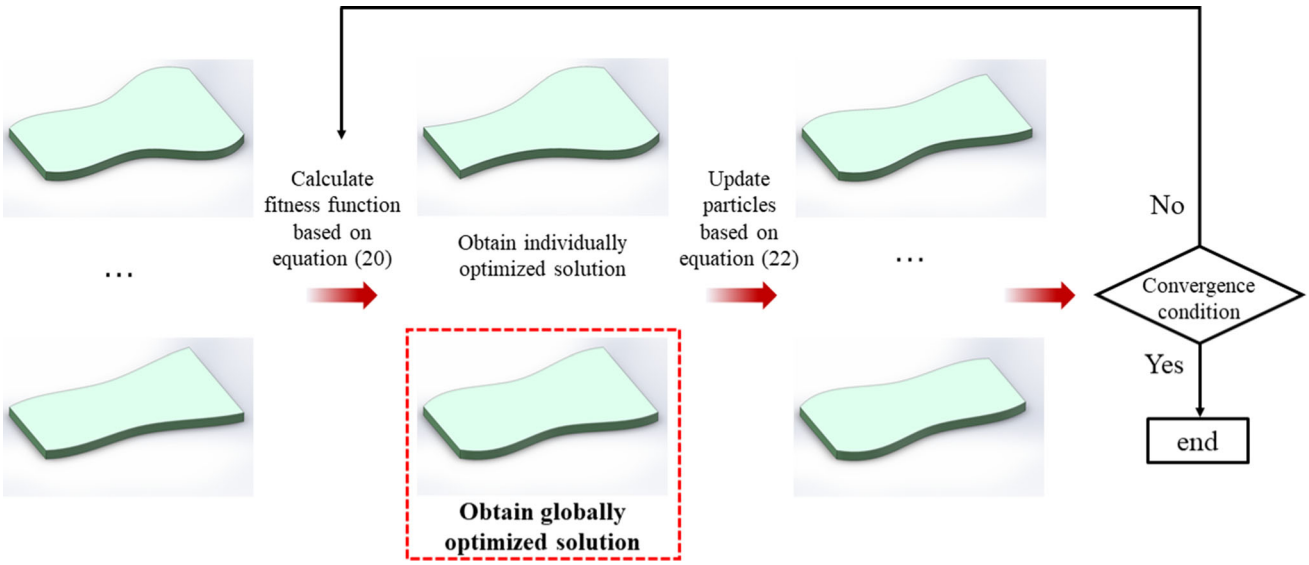

Fig. 2 The flowchart of PSO process

Table 1 The material properties of PZT-5H and Brass

	$\rho(\mathrm{kg}\cdot\mathrm{m}^{-3})$	$\bar{c}_{11}(\mathrm{GPa})$	$\bar{c}_{12}(\mathrm{GPa})$	$\bar{c}_{66}(\mathrm{GPa})$	$\bar{e}_{31}(\mathrm{C}\cdot\mathrm{m}^{-2})$	$\bar{\varepsilon}^{S}_{33}(\mathrm{F}\cdot\mathrm{m}^{-1})$
PZT-5H	7500	66.2	19.2	23.5	−23.4	17.3E−9
Brass	9000	105	–	–	–	–

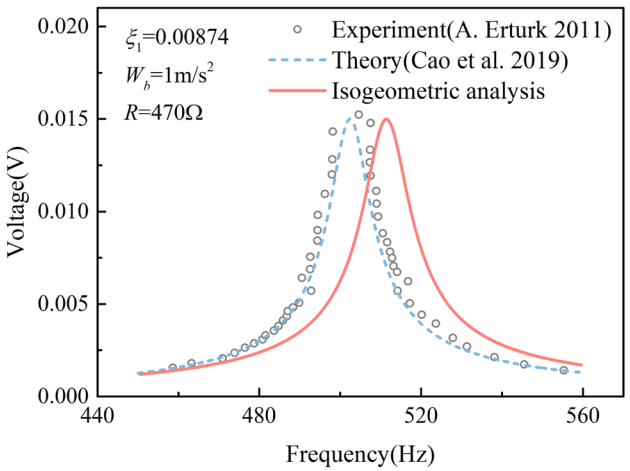

Fig. 3 The frequency response of the output voltage with different models

theoretical values (Cao et al. 2019) and IGA results. It can be seen that the output voltage amplitude is all 0.015V, and the experimental and theoretical values of the resonant frequency are both around 502Hz. The numerical result is 511Hz, the errors are within 2%. Therefore, the IGA model is validated by the experimental and theoretical values.

To study the convergence of the IGA model, we define an error parameter error $= |\omega_1 - \omega_1^*|/\omega_1^*$, where ω_1 is calculated by IGA, and a reference solution ω_1^* is obtained from theoretical value about the first natural frequency. The variation curves of error with the number of elements are described in Fig. 4 for various orders $p = 2, 3, 4, 5, 6$. The results show that the parameter error gradually decreases as the number of elements increases with a given element order, and the minimum value of error is 1.52%. Meanwhile, error also decreases with the increase of the element orders. Particularly, when $p > 5$, within a given range of the number of elements, no obvious improvement in the accuracy or convergence rate is observed. Furthermore, as the element orders and the number of elements increase, the calculation cost increases by multiples. Therefore, considering the accuracy and calculation cost, the following examples use quadratic element ($p = q = 2$) to discretize the structure.

Compared with finite element analysis, another advantage of IGA is that it can accurately describe the analysis model. In order to evaluate performance of IGA for a complex geometry, we analyze a curved PEH as displayed in Fig. 5. The damping ratio is set as $\xi_1 = 0.00874$, and 24×16 quadratic elements are utilized. Figure 6 sketches the numerical solutions and COMSOL simulation results of the open-circuit voltage. The detailed simulation process has been described in the literature (Cao et al. 2020), which will not be repeat here. At the same time, the frequency response of the above rectangular model is also given.

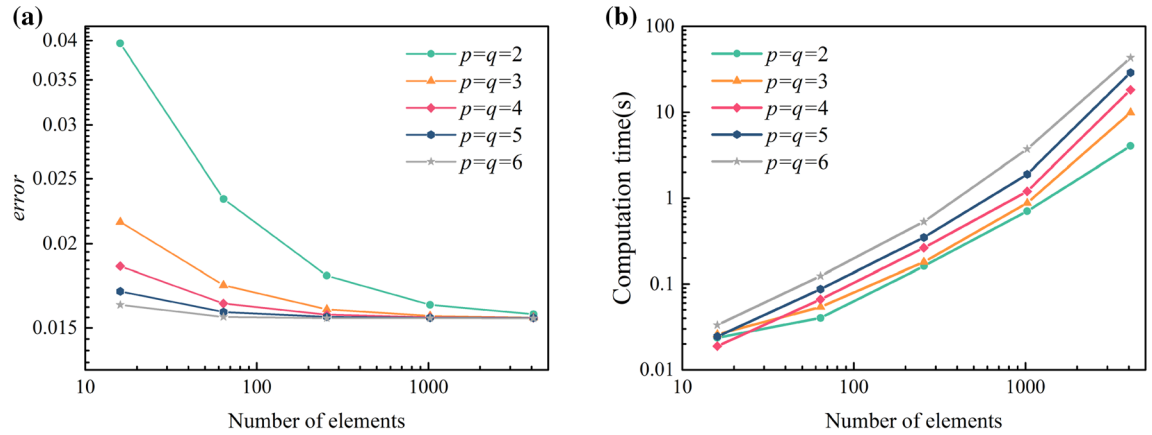

Fig. 4 The variation curve with different element orders **a** error vs the number of elements; **b** computation time vs the number of elements

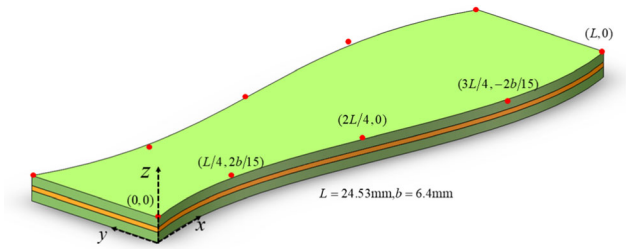

Fig. 5 A curved PEH with initial knots vectors $\Xi_\xi = \{0,0,0,1/3,2/3,1,1,1\}, \Xi_\eta = \{0,0,1,1\}$

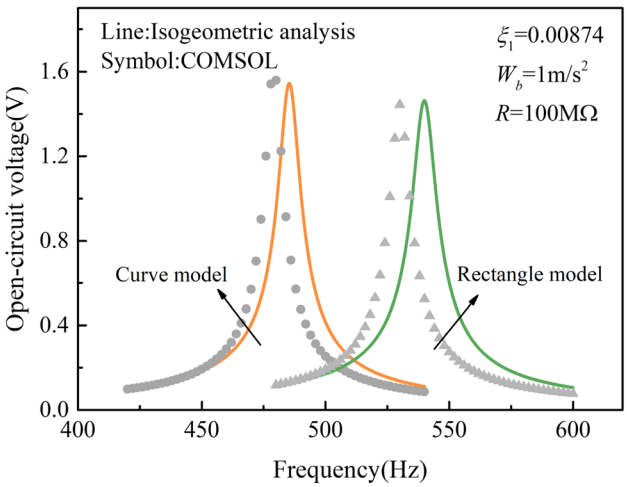

Fig. 6 The frequency responses of the open-circuit voltage

For the rectangular model, the numerical solutions and simulation results of the open-circuit voltage amplitude are 1.46 and 1.44V, respectively. As for the curved model, the open-circuit voltage amplitudes are respectively 1.57 and 1.56V, and the errors are within 1.5%. Thus, the IGA model is further validated by COMSOL simulation. In addition, the open-circuit voltage amplitude of the curved model increases by 7.5%, compared with the rectangular model. The resonant frequency reduces from 539.4 to 485.5Hz, and there is a 10% change. Therefore, it can be concluded that the shape design of PEH can adjust resonant frequency and enhance energy efficiency, Sect. 4.2 will discuss shape optimization in detail.

4.2 Numerical examples

We compare the computational efficiency and convergence speed of PSO and GA, and then combine IGA and PSO to study the shape optimization of PEH, and explore the effect of thickness ratio h_s/h_p and frequency constraint on the optimized designs in this subsection. The numerical examples mainly aim at the three structures of different geometric boundaries as shown in Fig. 7, where the thickness of piezoelectric layer and metal layer is $h_p = 0.265$ mm, $h_s = 0.14$ mm. The first structure is a rectangle design, named as Model A, defined by length L and width b. The second structure is represented by a trapezoid, identified as Model B. Here, the boundary is described by the parameter α under the premise of $L = 24.53$ mm, $b = 6.4$ mm. The third geometry corresponds to a curved boundary (Model C in Fig. 7), which is described by control points (red points). The design variables are set as the coordinates of the control points, and $L = 24.53$ mm, $b = 6.4$ mm remains unchanged. It is noted that upper and lower boundaries are symmetric with respect to middle line. Furthermore, since we are interested in the resonant behavior, the variation of mechanical damping is also important. Thus, it is assumed that the damping ratios from Eq. (15) are set as $\xi_1 = 0.00874$, $\xi_2 = 0.01$ for the following examples.

By default, the parameters of PSO are set as $\tilde{\omega}_{\min} = 0.4, \tilde{\omega}_{\max} = 0.8, c_1 = c_2 = 1.5, N = T_{\max} = 100$. GA is an evolutionary optimization methodology by mimicking biological evolution, which contains encode,

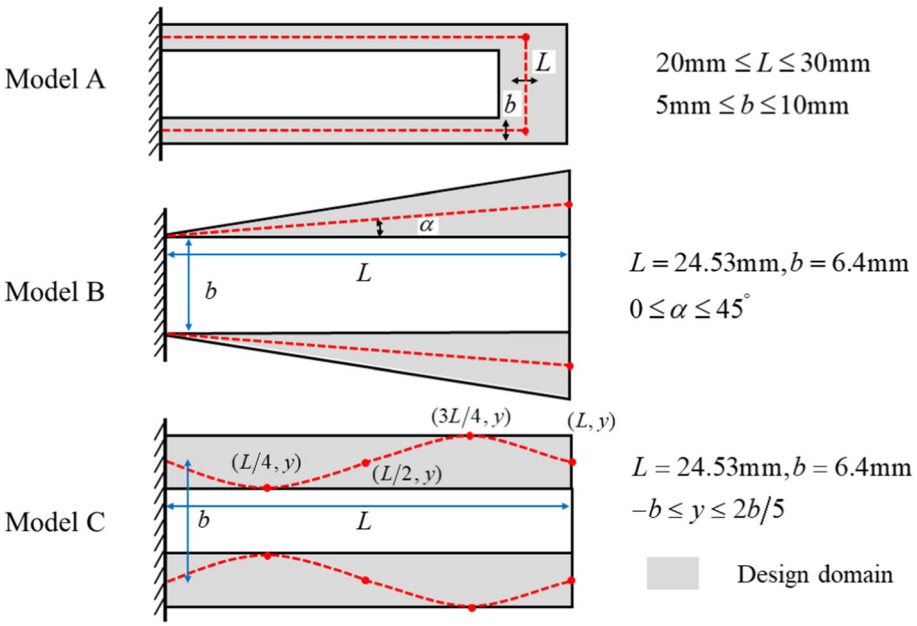

Fig. 7 Three different models of PEH: rectangular (Model A), trapezoidal (Model B), curved (Model C) plate

decode, selection, crossover and mutation for searching and optimizing complex problems, and the relevant theory can refer to the literature (Nabavi and Zhang 2017, 2019). The parameters of GA are following for comparison: the population size is set as 100, and roulette wheel selection with a 0.8 crossover rate is utilized to selection operation. A fixed mutation rate 0.01 is implement. All examples are completed at a personal computer with Intel Core i7-6700 CPU @3.30 GHz and 24 GB RAM.

4.2.1 Comparative analysis

Firstly, we take maximum average open-circuit voltage as the objective function and compare the computational efficiency and convergence speed of PSO and GA based on the three groups of models. The range of design variables is shown in Fig. 7, the design variables of Model A are L and b, and the geometry is discretized by 32×16 quadratic elements. The range of angle α is $[0^{\circ}, 45^{\circ}]$ for Model B, and the domain is discretized by a mesh of 24×16 elements. For Model C, the ordinates of the control points belong to $[-b, 2b/5]$, and the mesh number of Model C is the same as Model B. The maximum velocities of particle are respectively set as 0.001, 4 and 0.0005 in the PSO, and the number of binary codes is respectively 19,13 and 20 for Model A, B and C. These problems will be solved by both the PSO and GA, five times each, to implement the comparative analysis in the following section.

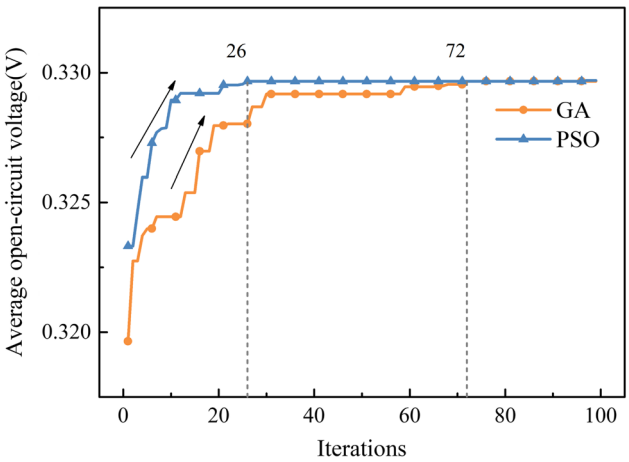

Fig. 8 The convergence history of Model A with different optimization methods

The results show that each optimized designs of the same geometric configuration are identical, where the optimized design for Model A is $L = 30$ mm, $b = 10$ mm, and the optimized angle corresponding to Model B is $\alpha = 45^{\circ}$ and the coordinates of optimized control points are $(L/4, -4.6), (L/2, 1.3), (3L/4, -6.3), (L, -6.4)$. Table 2 summarizes the optimized value and average computation

Table 2 The comparison about optimized values and computation time

Optimized model/methods	Model A		Model B		Model C	
	PSO	GA	PSO	GA	PSO	GA
The objective values	0.329	0.329	0.361	0.361	0.306	0.306
Computation time(s)	9980.7	10,631.7	8218.8	8660.3	8199.4	8721.7

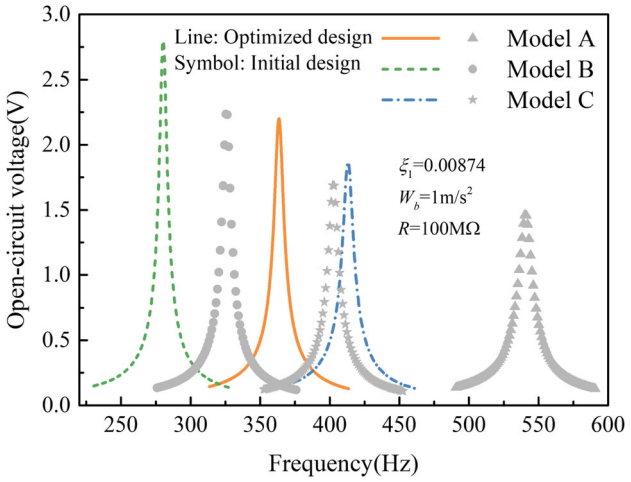

Fig. 9 The frequency responses of the open-circuit voltage with different models

time. It is shown that different optimization methods obtain the same optimized values, and the total computation time of PSO is reduced by 6% compared with GA, and saving calculation resources.

To further compare the convergence speed, it can be observed from Fig. 8 that the initial value of gbest for PSO is greater than that of GA, and PSO rapidly converges to the stable value within approximately first 26 iterations, while GA needs 72 iterations. Therefore, the numerical examples prove that PSO has better computational efficiency and convergence performance than GA. The similar conclusion were obtained by a set of benchmark test problems (Hassan et al. 2005). In the following examples, PSO will be utilized to study the influence of material thickness ratio h_s/h_p and frequency constraint on the optimized results.

4.2.2 Maximum average open-circuit voltage

According to the optimized results from Sect. 4.2.1, Fig. 9 sketches the frequency responses of the open-circuit voltage for the initial designs and optimized designs. It is indicated that the open-circuit voltage amplitudes of the initial design and optimized design for Model A are respectively 1.46 and 2.21V. Compared with the initial design, the open-circuit voltage amplitude of the optimized design increases by 51.4%. For Model B, the open-circuit voltage amplitude of the initial design with $\alpha = 30^{\circ}$ is 2.24V, but that of the optimized design is 2.82V, which increases by 25.9%. The same conclusion for Model C is obtained, namely, the open-circuit voltage amplitude of the optimized design increases by 11.2%, compared with the initial design with $(L/4, b/3), (L/2, 0), (3L/4, -b/3), (L, 0)$. Furthermore, the growth rates of the open-circuit voltage amplitude have a relationship of Model A > Model B > Model C. Additionally, the growth rates of objective value for three models are 2.2, 1.4, and 0.33%, and the magnitude relationship is the same as the growth rates of open-circuit voltage amplitude.

According to the average output power $P = \Phi^2/(2R)$, the comparison on the output power of PEH between the initial design and the optimized design is further performed. Note that the output power means the peak power under a given load resistance and frequency excitation in this paper. Table 3 summarizes the output power characteristics in detail and indicates that the optimized resistance of the optimized design is smaller than that of the initial design for the identical configuration, while the optimized resistance of Model B is one order of magnitude smaller than that of Model A and C. It can be recalled the optimized resistance formulation from the reference (Erturk and Inman 2011) that the optimized resistance is inversely proportional to the capacitance, that is $\overline{K}_{\phi\phi}$ in this paper. Numerical tests show that the $\overline{K}_{\phi\phi}$ of the optimized design increases by about 50% compared to the initial design for all models, and that of Model B is one order of magnitude lager than Model A and Model C. This is in good agreement with the optimized resistance. Additionally, maximum output power of the optimized design for Model A increases by 184.7%, and the power density increases by 36.4%, compared with the initial design. Meanwhile, Model A maintains the largest increase. Especially, regardless of the initial design and optimized design, maximum output power of Model B is 3–5 times larger than the other two. It is worthy of our attention that maximum output power of Model C increases by 92.8%, but the power density decreases by 4.4%. The main reason is that the volume of the optimized design is almost doubled.

Later on, the thickness of piezoelectric layer $h_p = 0.265$ mm is unchanged, and the thickness ratio h_s/h_p are respectively set as $(20:53), (1:1), (2:1)$. The optimized results of Model A and Model B are not affected by the thickness ratio, that is, the optimized dimensions of Model A are $L = 30$ mm, $b = 10$ mm, and the optimized angle is $\alpha = 45^{\circ}$ for Model B. However, the optimized results of Model C are illustrated in Fig. 10, it can be observed that the geometry shapes are generally similar, and only the coordinates of the second and third control points are slightly different.

We take Model C as an example to investigate the frequency responses based on Eq. (18),

Table 4 summarizes the resonant frequency and open-circuit voltage amplitude of the initial designs and the optimized designs. It is known that the open-circuit voltage amplitude decreases with the increase of thickness ratios, and the open-circuit voltage amplitude of the optimized designs are about 12% higher than that of the initial

Table 3 The power characteristics of different models

Models	Optimized resistance (kΩ)	Maximum output power (μW)	Power density ($\mu W/\text{mm}^3$)
Model A			
Initial design	245	1.11	0.011
Optimized design	201	3.16(+184.7%)	0.015(+36.4%)
Model B			
Initial design	89	7.21	0.0213
Optimized design	81	13.0(+80.3%)	0.0256(+20.2%)
Model C			
Initial design	221	1.66	0.0158
Optimized design	141	3.20(+92.8%)	0.0151(−4.4%)

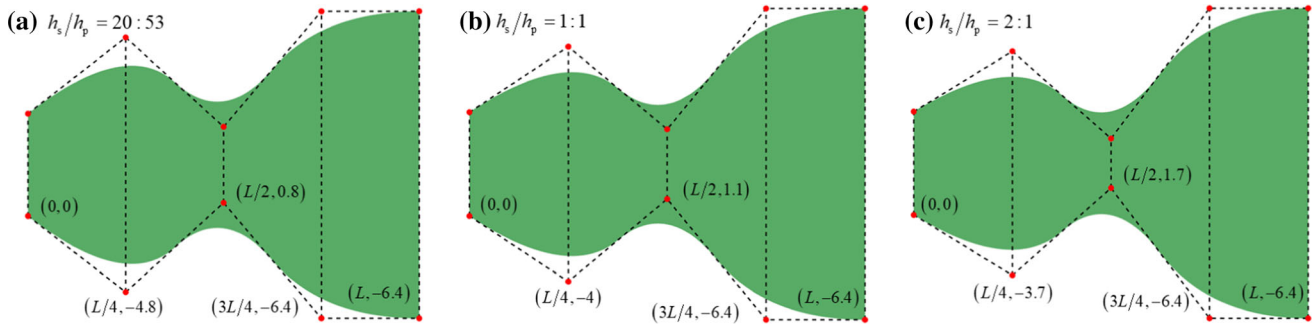

Fig. 10 The optimized results of Model C with different thickness ratios

Table 4 The characteristics of electric response with different models

Models	$h_s/h_p = 20:53$		$h_s/h_p = 1:1$		$h_s/h_p = 2:1$	
	Initial design	Optimized design	Initial design	Optimized design	Initial design	Optimized design
Resonant frequency (Hz)	379.0	386.7	476.4	473.1	643.3	624.4
Open-circuit voltage amplitude (V)	1.72	1.92 (+11.6%)	1.58	1.78 (+12.7%)	1.35	1.55 (+14.8%)

designs. Additionally, the resonant frequency increases gradually as the thickness ratios increase, and its variation range is up to 69.7%, so adjusting natural frequency can be realized by changing the thickness ratio.

To further explore the effectiveness of the optimized designs, the variation of the output power with load resistance is described in Fig. 11. Considering that the variation rules of different thickness ratios are the same, we take $h_s/h_p = 1:1$ as an example to explain in detail. The optimized resistances of optimized design and initial design are respectively 125kΩ, 189kΩ, and the corresponding maximum output powers are 3.25 μW, 1.7 μW. In other words, the maximum output power of the optimized design is about twice as high as that of the initial design. Moreover, the maximum output powers increase with the increase of thickness ratios, and the optimized resistances decrease. The numerical laws of Model A and Model B are the same as those above and will not be described here.

In short, numerical examples show that PSO has better computational efficiency and convergence performance than GA. Although the three models are different in shape and size, the non-traditional design can further improve the performance of PEH, such as Model B and Model C. The thickness ratios have little effect on the optimized geometry, and we can adjust the resonant frequency by change the thickness ratios, so as to realize high harvesting efficiency.

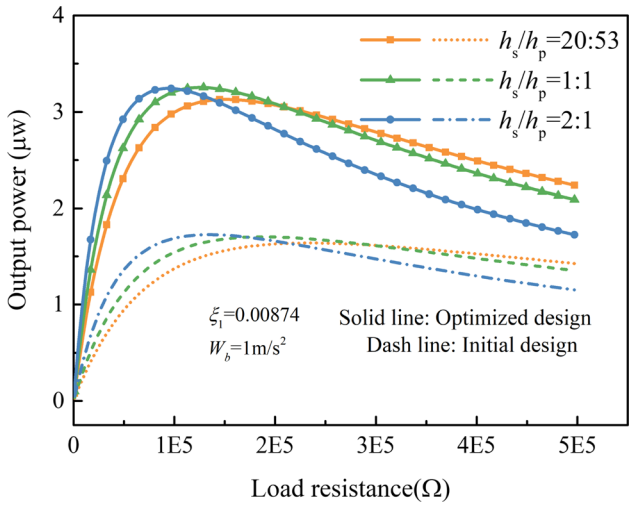

Fig. 11 The variation of the output power with load resistance at the open-circuit resonant frequency

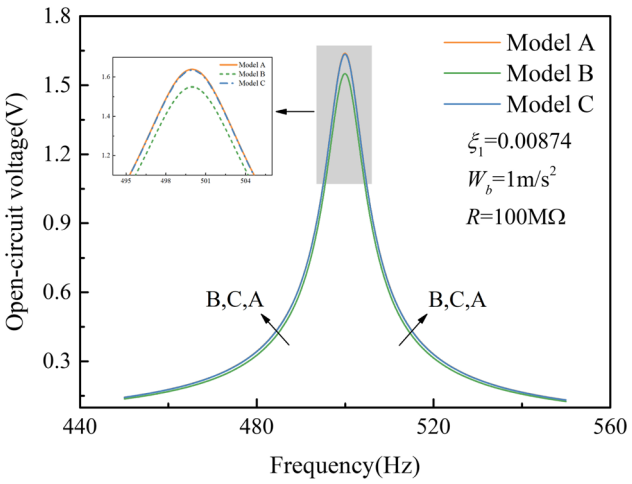

Fig. 12 The frequency responses of the open-circuit voltage with optimized designs

4.2.3 Maximum average open-circuit voltage with frequency constraint

According to the analysis results of Sect. 4.2.2, the range of resonant frequency for different models is 280–643 Hz. For the vibrational sources with different frequencies, on the one hand, we can optimize the geometric shape to enhance the energy efficiency. On the other hand, when the geometric shape has reached the optimized electric responses in the identical configuration, the thickness ratio can be further changed to adjust the natural frequency, so as to enhance energy efficiency. Therefore, the optimization model c_2 is performed, and the influence of the thickness ratio and frequency constraint on optimized designs is investigated.

The penalty function method is used to solve the optimization formulation, and the choice of the penalty factor is crucial. According to the numerical relationship between the objective function and constraint function, we take the penalty factors as -0.01 in this paper. The parameters are set as $\omega_{obj} = 1000\pi(\text{rad/s}), \delta = 10\pi(\text{rad/s})$, the remaining parameters are the same as Sect. 4.2.1. Consequently, the optimized dimensions of Model A are $L = 25.6$ mm, $b = 9.9$ mm, and the optimized angle is $\alpha = 2.2^{\circ}$ for Model B, and the coordinates of control points for Model C are $(L/4, -4.3), (L/2, -0.8), (3L/4, 1.5), (L, -6.3)$. Correspondingly, the frequency responses of the open-circuit voltage for the above optimized design are depicted in Fig. 12.

It can be observed that the resonant frequency of the optimized designs is near 499.5 Hz, which meet the constraint condition. In addition, the open-circuit voltage amplitudes are 1.64, 1.55, and 1.63V, respectively. Compared with the optimized results from Fig. 9, the open-circuit voltage amplitudes have a downward trend, and the maximum reduction is 45.0% of Model B. Moreover, the open-circuit voltage amplitude of Model A increases by 12.3%, while that of Model B and Model C respectively decreases by 30.8 and 3.6% compared to the initial design.

Considering the design space, we take Model C as example to analyze shape optimization of PEH under different frequency constraints and thickness ratios. Firstly, the thickness of piezoelectric layer and metal layer are respectively $h_p = 0.265$ mm, $h_s = 0.14$ mm, the objective frequency are set as 800 and $1200\pi(\text{rad/s})$. Figure 13 displays the frequency responses of the open-circuit voltage, it can be seen that the resonant frequency of the optimized designs meets the design requirements, and the open-circuit voltage amplitudes are 1.91 and 1.37V respectively. Furthermore, combined with the optimized results in Fig. 12, it is concluded that the open-circuit

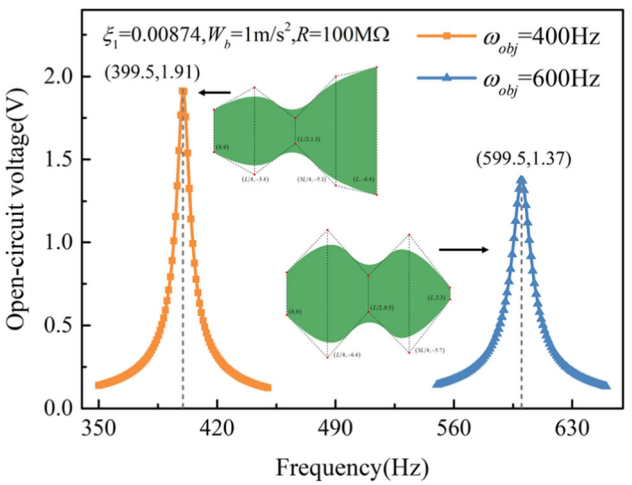

Fig. 13 The frequency responses of the open-circuit voltage with optimized designs

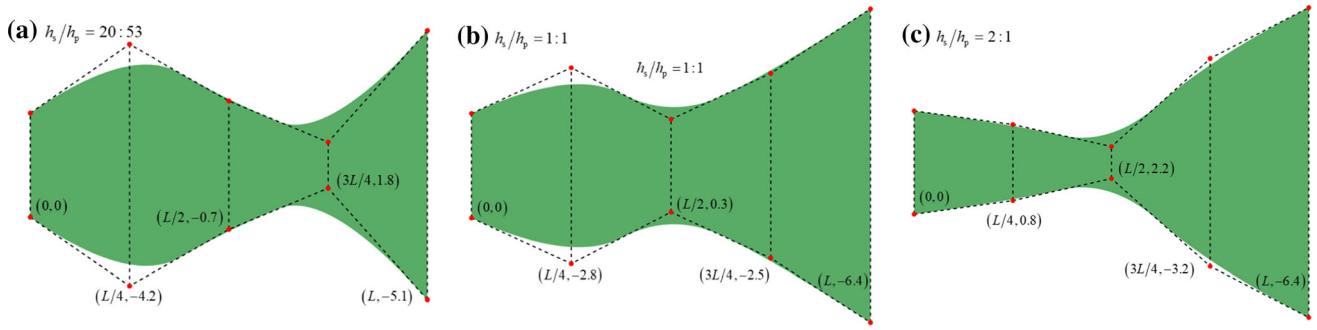

Fig. 14 The optimized designs of Model C with different thickness ratio

voltage amplitude decreases with the increase of frequency constraint, and the optimized shape of the three is quite different.

The thickness of piezoelectric layer is set as $h_p = 0.265$ mm, and the objective frequency is $1000\pi(\text{rad/s})$. The optimized designs for the thickness ratio $(20:53), (1:1), (2:1)$ are obtained as shown in Fig. 14. The thickness ratios have a great influence on the optimized shape, that is, as the thickness ratio increases, the material area of the fixed edge gradually decreases, and that of the free edge increases. Particularly, the optimized shape of thickness ratio $(2:1)$ is significantly different from that of the first two.

Based on Eq. (18), it is found that the resonant frequency is all 499.5 Hz, meeting the frequency constraint condition, and the open-circuit voltage amplitudes of the optimized designs are 1.57, 1.72 and 1.69V, respectively. The variations of the output power with load resistance are shown in Fig. 15 for the optimized designs, it can be observed that the maximum output power increases with the increase of the thickness ratios, and the values are respectively $1.53, 2.53, 2.92\ \mu W$. Compared with the initial designs from Fig. 11, the optimized designs of the thickness ratio $(1:1), (2:1)$ increase by 48.8 and 68.8%, but the optimized design of $h_s/h_p = (20:53)$ decreases by 6.7%. More importantly, maximum output powers have a downward trend compared with the optimized designs from Fig. 11, and the maximum reduction is 51.1% of case $h_s/h_p = (20:53)$.

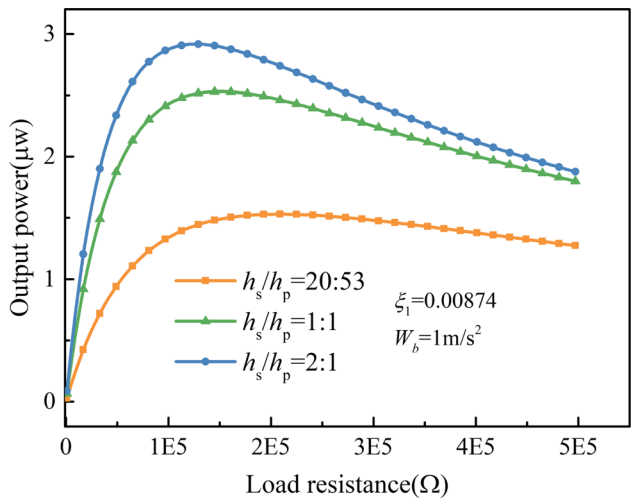

Fig. 15 The variation of the output power with load resistance at the open-circuit resonant frequency

5 Conclusions

In this paper, we derive the IGA formulation of a bimorph PEH based on the Kirchhoff–Love plate theory. Then two optimization models with maximum average open-circuit voltage as the objective function are discussed. The IGA model is well verified with the datum from the literature, and the comparison analysis between PSO and GA is fully implemented in view of computational efficiency and convergence speed. Several numerical examples are performed to investigate the effect of the thickness ratio and frequency constraint on the optimized shape. Several prime conclusions can be summarized as follows.

The shape optimization method based on IGA and PSO has the advantages of high computational efficiency and fast convergence speed. When the frequency constraint is not considered, the open-circuit voltage amplitude increases by 51.4%, and the maximum output power increases by 184.7%, compared with the initial design. Furthermore, compared with the rectangular design of Model A, the non-traditional design can further improve the energy harvesting efficiency, such as Model B and Model C. More importantly, in addition to considering the frequency constraint, the free vibration characteristics of the structure can be adjusted by changing the thickness ratio to harvest energy with resonant state.

As with the majority of studies, the design of the current study is subject to limitations. For instance, the IGA model is derived based on Kirchhoff–Love plate theory, which is only suitable for thin plate. The numerical examples in this paper do not consider the effect of variable thickness and

thickness optimization. To further extend this model, we can apply higher-order shear deformation theory to calculate power generation by PEH and carry out the shape optimization of thick PEH. Furthermore, based on a generalized shear deformation theory and IGA framework, we can simultaneously optimize the thickness and shape profiles of PEH.

Declarations

Conflict of interest The authors declare that they have no conflict of interest.

References

Akbar M, Curiel-Sosa JL (2018) Evaluation of piezoelectric energy harvester under dynamic bending by means of hybrid mathematical/isogeometric analysis. Int J Mech Mater Des 14:647–667. https://doi.org/10.1007/s10999-017-9395-0

American A, Standard N (1984) An American National Standard: IEEE Standard on Piezoelectricity. IEEE Trans Sonics Ultrason 31:8–10. https://doi.org/10.1109/T-SU.1984.31464

Benson D, Bazilevs Y, Luycker ED, Hsu M (2010) A generalized finite element formulation for arbitrary basis functions: From isogeometric analysis to XFEM. Int J Numer Methods Eng 83:765–785

Bhavikatti SS, Ramakrishnan CV (1980) Optimum shape design of rotating disks. Comput Struct 11:397–401. https://doi.org/10.1016/0045-7949(80)90105-4

Bourisli RI, Al-Ajmi MA (2010) Optimization of smart beams for maximum modal electromechanical coupling using genetic algorithms. J Intell Mater Syst Struct 21:907–914. https://doi.org/10.1177/1045389X10370544

Bui TQ (2015) Extended isogeometric dynamic and static fracture analysis for cracks in piezoelectric materials using NURBS. Comput Methods Appl Mech Eng 295:470–509. https://doi.org/10.1016/j.cma.2015.07.005

Bui TQ, Hirose S, Zhang C et al (2016) Extended isogeometric analysis for dynamic fracture in multiphase piezoelectric/piezomagnetic composites. Mech Mater 97:135–163. https://doi.org/10.1016/j.mechmat.2016.03.001

Calderon Hurtado A, Peralta P, Ruiz RO et al (2022) Shape optimization of piezoelectric energy harvesters of variable thickness. J Sound Vib 517:116503. https://doi.org/10.1016/j.jsv.2021.116503

Cao Y, Huang H, Zhu ZH, Su S (2019) Optimized energy harvesting through piezoelectric functionally graded cantilever beams. Smart Mater Struct 28:025038. https://doi.org/10.1088/1361-665X/aaf761

Cao Y, Huang H, He W (2020) Energy harvesting characteristics of preloaded piezoelectric beams. J Phys D Appl Phys 53:095501. https://doi.org/10.1088/1361-6463/ab5a05

Cho S, Ha SH (2009) Isogeometric shape design optimization: exact geometry and enhanced sensitivity. Struct Multidiscip Optim 38:53–70. https://doi.org/10.1007/s00158-008-0266-z

Dietl JM, Garcia E (2010) Beam shape optimization for power harvesting. J Intell Mater Syst Struct 21:633–646. https://doi.org/10.1177/1045389X10365094

Erturk A, Inman DJ (2009) An experimentally validated bimorph cantilever model for piezoelectric energy harvesting from base excitations. Smart Mater Struct 18:025009. https://doi.org/10.1088/0964-1726/18/2/025009

Erturk M, Inman DJ (2011) Piezoelectric energy harvesting. Wiley, Hoboken

Fourie PC, Groenwold AA (2002) The particle swarm optimization algorithm in size and shape optimization. Struct Multidiscip Optim 23:259–267. https://doi.org/10.1007/s00158-002-0188-0

Francavilla A, Ramakrishnan CV, Zienkiewicz OC (1975) Optimization of shape to minimize stress concentration. J Strain Anal Eng Des 10:63–70. https://doi.org/10.1243/03093247V102063

Gao J, Xiao M, Zhang Y, Gao L (2020) A comprehensive review of isogeometric topology optimization: methods, applications and prospects. Chin J Mech Eng 33:1–28. https://doi.org/10.1186/s10033-020-00503-w

Ghoddus H, Kordrostami Z (2018) Harvesting the ultimate electrical power from MEMS piezoelectric vibration energy harvesters: an optimization approach. IEEE Sens J 18:8667–8675. https://doi.org/10.1109/JSEN.2018.2867552

Ha YD (2015) Generalized isogeometric shape sensitivity analysis in curvilinear coordinate system and shape optimization of shell structures. Struct Multidiscip Optim 52:1069–1088. https://doi.org/10.1007/s00158-015-1297-x

Hassan R, Cohanim B, De Weck O, Venter G (2005) A comparison of particle swarm optimization and the genetic algorithm. Collect Tech Pap - AIAA/ASME/ASCE/AHS/ASC Struct Struct Dyn Mater Conf 2:1138–1150. https://doi.org/10.2514/6.2005-1897

Hughes TJR, Cottrell JA, Bazilevs Y (2005) Isogeometric analysis: CAD, finite elements, NURBS, exact geometry and mesh refinement. Comput Methods Appl Mech Eng 194:4135–4195. https://doi.org/10.1016/j.cma.2004.10.008

Igura N, Shimomura T, Harada K et al (1995) A proposal for rotating machineries analysis by considering the unknown equal potential condition on FEM. IEEE Trans Magn 31:1722–1724. https://doi.org/10.1109/20.376367

James K, Russell E (1995) Particle swarm optimization. Proc ICNN'95 - Int Conf Neural Networks 20:1942–1948. https://doi.org/10.1002/9780470612163

Kiendl J, Schmidt R, Wüchner R, Bletzinger KU (2014) Isogeometric shape optimization of shells using semi-analytical sensitivity analysis and sensitivity weighting. Comput Methods Appl Mech Eng 274:148–167. https://doi.org/10.1016/j.cma.2014.02.001

Kumar AV, Parthasarathy A (2011) Topology optimization using B-spline finite elements. Struct Multidiscip Optim 44:471–481. https://doi.org/10.1007/s00158-011-0650-y

Kundu S, Nemade HB (2021) Piezoelectric vibration energy harvester with tapered substrate thickness for uniform stress. Microsyst Technol 27:105–113. https://doi.org/10.1007/s00542-020-04922-6

Le TC, Phung-Van P, Thai CH et al (2018) Isogeometric analysis of functionally graded carbon nanotube reinforced composite nanoplates using modified couple stress theory. Compos Struct 184:633–649. https://doi.org/10.1016/j.compstruct.2017.10.025

Lee SW, Cho S (2015) Isogeometric configuration design optimization of built-up structures. Struct Multidiscip Optim 51:319–331. https://doi.org/10.1007/s00158-014-1131-x

Li C, Han Q (2020) Guided waves propagation in sandwich cylindrical structures with functionally graded graphene-epoxy core and piezoelectric surface layers. J Sandw Struct Mater 9:1099636220959034. https://doi.org/10.1177/1099636220959034

Li C, Han Q, Wang Z, Wu X (2020) Analysis of wave propagation in functionally graded piezoelectric composite plates reinforced with graphene platelets. Appl Math Model 81:487–505. https://doi.org/10.1016/j.apm.2020.01.016

Liu Y, Lin S, Li Y et al (2019) Numerical investigation of Rayleigh waves in layered composite piezoelectric structures using the

SIGA-PML approach. Compos Part B Eng 158:230–238. https://doi.org/10.1016/j.compositesb.2018.09.037
Liu T, Li C, Wang C et al (2020) A simple-fsdt-based isogeometric method for piezoelectric functionally graded plates. Mathematics 8:1–24. https://doi.org/10.3390/math8122177
Mostafa Shaaban A, Anitescu C, Atroshchenko E, Rabczuk T (2020) Shape optimization by conventional and extended isogeometric boundary element method with PSO for two-dimensional Helmholtz acoustic problems. Eng Anal Bound Elem 113:156–169. https://doi.org/10.1016/j.enganabound.2019.12.012
Nabavi S, Zhang L (2017) Design and optimization of piezoelectric MEMS vibration energy harvesters based on genetic algorithm. IEEE Sens J 17:7372–7382. https://doi.org/10.1109/JSEN.2017.2756921
Nabavi S, Zhang L (2019) Nonlinear multi-mode wideband piezoelectric MEMS vibration energy harvester. IEEE Sens J 19:4837–4848. https://doi.org/10.1109/JSEN.2019.2904025
Nagy AP, Abdalla MM, Gürdal Z (2010a) Isogeometric sizing and shape optimisation of beam structures. Comput Methods Appl Mech Eng 199:1216–1230. https://doi.org/10.1016/j.cma.2009.12.010
Nagy AP, Abdalla MM, Gürdal Z (2010b) On the variational formulation of stress constraints in isogeometric design. Comput Methods Appl Mech Eng 199:2687–2696. https://doi.org/10.1016/j.cma.2010.05.012
Nagy AP, Ijsselmuiden ST, Abdalla MM (2013) Isogeometric design of anisotropic shells: optimal form and material distribution. Comput Methods Appl Mech Eng 264:145–162. https://doi.org/10.1016/j.cma.2013.05.019
Nguyen-Quang K, Vo-Duy T, Dang-Trung H, Nguyen-Thoi T (2018) An isogeometric approach for dynamic response of laminated FG-CNT reinforced composite plates integrated with piezoelectric layers. Comput Methods Appl Mech Eng 332:25–46. https://doi.org/10.1016/j.cma.2017.12.010
Nikoei S, Hassani B (2019) Isogeometric analysis of laminated smart shell structures covered with piezoelectric sensors and actuators using degenerated shell formulation. J Intell Mater Syst Struct 30:1913–1931. https://doi.org/10.1177/1045389X19849264
Nikoei S, Hassani B (2020) Study of the effects of shear piezoelectric actuators on the performance of laminated composite shells by an isogeometric approach. J Sandw Struct Mater. https://doi.org/10.1177/1099636220942911
Nisanth A, Suja KJ, Seena V (2021) Design and optimization of MEMS piezoelectric energy harvester for low frequency applications. Microsyst Technol 27:251–261. https://doi.org/10.1007/s00542-020-04944-0
Peralta P, Ruiz RO, Natarajan S, Atroshchenko E (2020) Parametric study and shape optimization of piezoelectric energy harvesters by isogeometric analysis and kriging metamodeling. J Sound Vib 484:115521. https://doi.org/10.1016/j.jsv.2020.115521
Phung-Van P, De Lorenzis L, Thai CH et al (2015a) Analysis of laminated composite plates integrated with piezoelectric sensors and actuators using higher-order shear deformation theory and isogeometric finite elements. Comput Mater Sci 96:495–505. https://doi.org/10.1016/j.commatsci.2014.04.068
Phung-Van P, Nguyen LB, Tran LV et al (2015b) An efficient computational approach for control of nonlinear transient responses of smart piezoelectric composite plates. Int J Non Linear Mech 76:190–202. https://doi.org/10.1016/j.ijnonlinmec.2015.06.003
Piegl L, Tiller W (1997) The NURBS book. Springer, Berlin
Qian X (2010) Full analytical sensitivities in NURBS based isogeometric shape optimization. Comput Methods Appl Mech Eng 199:2059–2071. https://doi.org/10.1016/j.cma.2010.03.005
Salmani H, Rahimi GH, Saraygord Afshari S (2019) Optimization of the shaping function of a tapered piezoelectric energy harvester using tabu continuous ant colony system. J Intell Mater Syst Struct 30:3025–3035. https://doi.org/10.1177/1045389X19873391
Seo YD, Kim HJ, Youn SK (2010) Shape optimization and its extension to topological design based on isogeometric analysis. Int J Solids Struct 47:1618–1640. https://doi.org/10.1016/j.ijsolstr.2010.03.004
Singh SK, Singh IV (2020) Analysis of cracked functionally graded piezoelectric material using XIGA. Eng Fract Mech 230:107015. https://doi.org/10.1016/j.engfracmech.2020.107015
Sun SH, Yu TT, Nguyen TT et al (2018) Structural shape optimization by IGABEM and particle swarm optimization algorithm. Eng Anal Bound Elem 88:26–40. https://doi.org/10.1016/j.enganabound.2017.12.007
Sunithamani S, Lakshmi P, Eba Flora E (2013) PZT length optimization of MEMS piezoelectric energy harvester with a non-traditional cross section: simulation study. Microsyst Technol 20:2165–2171. https://doi.org/10.1007/s00542-013-1920-y
Tabatabaei SMK, Behbahani S, Rajaeipour P (2016) Multi-objective shape design optimization of piezoelectric energy harvester using artificial immune system. Microsyst Technol 22:2435–2446. https://doi.org/10.1007/s00542-015-2605-5
Townsend S, Grigg S, Picelli R et al (2019) Topology optimization of vibrational piezoelectric energy harvesters for structural health monitoring applications. J Intell Mater Syst Struct 30:2894–2907. https://doi.org/10.1177/1045389X19873392
Truong TT, Lee J, Nguyen-Thoi T (2021) Multi-objective optimization of multi-directional functionally graded beams using an effective deep feedforward neural network-SMPSO algorithm. Struct Multidiscip Optim 63:2889–2918. https://doi.org/10.1007/s00158-021-02852-z
Wall WA, Frenzel MA, Cyron C (2008) Isogeometric structural shape optimization. Comput Methods Appl Mech Eng 197:2976–2988. https://doi.org/10.1016/j.cma.2008.01.025
Wang Y, Wang Z, Xia Z, Poh LH (2018) Structural design optimization using isogeometric analysis: a comprehensive review. C - Comput Model Eng Sci 117:455–507
Willberg C, Gabbert U (2012) Development of a three-dimensional piezoelectric isogeometric finite element for smart structure applications. Acta Mech 223:1837–1850. https://doi.org/10.1007/s00707-012-0644-x
Yoon M, Choi MJ, Cho S (2015) Isogeometric configuration design optimization of heat conduction problems using boundary integral equation. Int J Heat Mass Transf 89:937–949. https://doi.org/10.1016/j.ijheatmasstransfer.2015.05.112

Publisher's Note Springer Nature remains neutral with regard to jurisdictional claims in published maps and institutional affiliations.